Birefringence induced Vernier effect in optical fiber modal interferometers for enhanced sensing

Li, Kaiwei; Zhang, Nan; Zhang, Nancy Meng Ying; Zhou, Wenchao; Zhang, Ting; Chen, Ming; Wei, Lei

2018

Li, K., Zhang, N., Zhang, N. M. Y., Zhou, W., Zhang, T., Chen, M., & Wei, L. (2018). Birefringence induced Vernier effect in optical fiber modal interferometers for enhanced sensing. Sensors and Actuators B: Chemical, 27516-24. doi:10.1016/j.snb.2018.08.027

https://hdl.handle.net/10356/80530

https://doi.org/10.1016/j.snb.2018.08.027

Birefringence induced Vernier effect in optical fiber modal interferometers for enhanced sensing

Kaiwei Li[a], Nan Zhang[a,b], Nancy Meng Ying Zhang[a,b], Wenchao Zhou[c], Ting Zhang[a], Ming Chen[d], Lei Wei[a,b,*]

[a]*School of Electrical and Electronic Engineering, Nanyang Technological University, 50 Nanyang Avenue, 639798, Singapore*

[b]*CINTRA CNRS/NTU/THALES, UMI3288, Research Techno Plaza, 50 Nanyang Drive, 637553, Singapore*

[c]*State Key Laboratory of Applied Optics, Changchun Institute of Optics, Fine Mechanics and Physics, Chinese Academy of Sciences, Changchun 130033, P. R. China*

[d]*Center for Photovoltaic Solar Energy Shenzhen Institutes of Advanced Technology Chinese Academy of Sciences Shenzhen 518055, P. R. China*

**Corresponding author: wei.lei@ntu.edu.sg*

Abstract:

We report a simple and effective method to improve the sensitivities of fiber-optic modal interferometers with birefringence induced Vernier effect. Taking optical microfiber coupler as an example, we study the sensitivity enhancement of a microfiber coupler for refractive index (RI) sensing both theoretically and experimentally in the RI range of 1.33-1.35 where bioassays are typically carried out. Numerical results show that by tracing the wavelength shifts of dips in the envelope formed by the Vernier effect, RI sensitivities can be improved by almost one order of magnitude compared to the sensors without the Vernier effect. Then we experimentally achieve an ultra-high sensitivity of 35823.3 nm/RIU using a microfiber coupler with a width of 3.2 μm. More importantly, we apply this ultra-sensitive sensor to detect human cardiac troponin, and a limit of detection of 1 ng/mL is achieved. This sensor is simple in configuration and can serve as a bio-photonic platform for clinical diagnostics environmental monitoring and food safety.

1. Introduction

Fiber-optic biosensors have been widely employed in the fields of clinical diagnosis [1,2] environmental monitoring [3] and food security [4,5] due to the merits of small footprint, short response time, immune to electromagnetic interferences, and capability of remote sensing. Thereinto, label-free fiber-optic biosensors are gaining increasing attention since the sensing procedure is simple, cost-effective, free of laborious labeling chemistry, and more importantly, they offer the capability for real-time monitoring of biochemical reaction [6,7].

Generally, the working principle of label-free optical biosensing is based on the modulation of the optical signals by the refractive index (RI) changes arising from the bio-recognition events at sensor surfaces [8]. Thus, fiber-optic RI sensors are the core element for label-free fiber-optic biosensors. Over the past decades, fiber-optic biosensors with different sensing mechanisms have been proposed and studied. For examples, optical fiber-based surface plasmon resonance (SPR) sensors [9] which are transformed from the golden standard prism-based SPR, have been well studied for both RI sensing and biosensing, and further evolved into several new sensing schemes [10,11]. Moreover, fiber-optic localized surface plasmon resonance (LSPR) biosensors which utilize the collective oscillation of the conduction electrons of nanoparticles, have also been well explored [12,13]. Evanescent wave based fiber-optic biosensor is another large class, which uses the evanescent wave of the guided modes to probe the bio-interactions at the bio-functionalized interfaces. Various sensing schemes such as microfiber interferometers [5,14], optical microfiber couplers (OMCs) [15,16], and long-period fiber gratings [6,17,18] have been adopted for both RI

sensing and biosensing. These sensors are simple in structure, cost-effective in fabrication and free of the complicated process of depositing noble metallic films or nanoparticles on the fiber surface.

Although multifarious label-free fiber-optic RI sensors and biosensors have been proposed and studied, the development and further applications of fiber-optic label-free biosensors have been limited by challenges in sensitivity, specificity, reproducibility, etc., while the sensitivity is the most crucial one [19]. In fact, most of the reported fiber-optic label-free biosensors only show limited RI sensitivities of about several-hundred nm per refractive index unit (nm/RIU) to several-thousand nm/RIU [10,16,17,20], which is difficult to meet the required sensing performance in biosensing [21]. To address the challenge of sensitivity, several methods have been developed. For example, the modal dispersion turning points have been discovered in long-period fiber gratings, optical microfiber interferometers and OMCs, benefiting from which the RI sensitivity can be improved to tens of thousands nm/RIU [15,22–25]. The Vernier effect has also been utilized in a cascaded optical microfiber ring resonator, and thanks to this effect, the RI sensitivity can be further improved [26]. These studies not only offer guidelines for developing ultra-sensitive fiber-optic RI sensors but also reveal the unprecedented potentials of employing such sensors for biosensing applications [27,28].

Though several pioneer studies on sensitivity improvement either by optimizing sensor parameters or by introducing new mechanisms have been reported. The Vernier effect resulted from the superposition of two modal interferences in two orthogonal polarizations in a birefringent optical fiber has not been explored for sensing enhancement. In this study, we take the OMC as an example and study the Vernier effect and sensitivity enhancement both theoretically and experimentally. We also draw a comparison of the sensing performances between the OMCs with and without the Vernier effect. Owing to the Vernier effect, the RI sensitivity can be increased by nearly one order of magnitude. As a proof-of-concept, we implement this OMC sensor into biomarker detection. Here, we employ human cardiac troponin T (cTnT) as a model analyte because it is an acknowledged biomarker for the diagnosis of acute myocardial infarction [29]. Again, we demonstrate that with the help of the Vernier effect, the wavelength shift response induced by biomolecule binding can be amplified and the sensing performance can be significantly improved. Compared with previously reported OMC sensors that can reach the equivalent ultra-high sensitivities by utilizing the dispersion turning point at single polarization state [15], the required waist width is a bit larger, which make the sensor more robust and stable to use.

2. Experimental

2.1 Reagents and materials

All experiments are performed with reagents of analytical reagent grade. NaOH solution is prepared by dissolving NaOH powder (Alfa Aesar) in deionized water (DI water). Poly (allylamine) (PAA) solution (Mw ~65000, 10 wt. % in H_2O) is purchased from Sigma-Aldrich (Singapore). Phosphate buffered saline (PBS, pH 7.4) solution is purchased from Vivantis (USA). Natural human cTnT protein and cTnT antibody are purchased from Abcam (Cambridge, MA). Bovine serum albumin (BSA) are obtained from Aladdin (Shanghai, China). RI solutions with different RI values are prepared by dissolving sodium chloride (NaCl, Affymetrix, 99+%) in DI water to different concentrations. The RI values are

measured using a digital refractometer (Reichert, USA). Standard single mode optical fibers (SMF-28e) are obtained from Corning Inc. (New York, USA).

2.2 Fabrication of OMCs

The OMCs are fabricated with standard single-mode optical fibers (Corning SMF-28) through a heating and pulling method [30]. Generally, two bare optical fibers are double twisted, along in parallel and fixed onto the elongation stages. A flame is used to heat the fibers and the width of the heating region is ~2 mm. Two electric motors pull the fibers in opposite directions at a controlled speed. To obtain couplers with long uniform waist and desirable length, the flame is scanned by a motor with controlled scanning distances. Thus, the waist width can be controlled by varying the duration of the tapering process. As the optical guiding property of the OMC is very sensitive to the width and length of the waist region, which requires the tapering setup to be quite sophisticated to achieve OMCs with the identical output spectra. Here, we employ an in-line monitoring method to monitor the output spectra in real-time during the fabrication process, which would increase the success rate considerably. To keep the coupler stable and robust, we fix the fabricated OMC inside a fluid channel on a specially designed Teflon sensor chip.

2.3 Experimental system for optical measurement

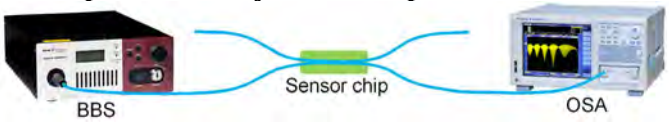

Fig. 1. Experimental setup for optical measurements.

The experimental setup used for optical measurement is shown in Fig. 1. A supercontinuum white light source (SuperK COMPACT, NKT Photonics) with the wavelength range of 450-2400 nm is used as a broadband source (BBS). The output transmission spectrum at the throughput port is acquired by an optical spectrum analyzer (OSA, Yokogawa AQ6370C) with a wavelength resolution of 0.02 nm.

2.4 Surface modification and antibody immobilization

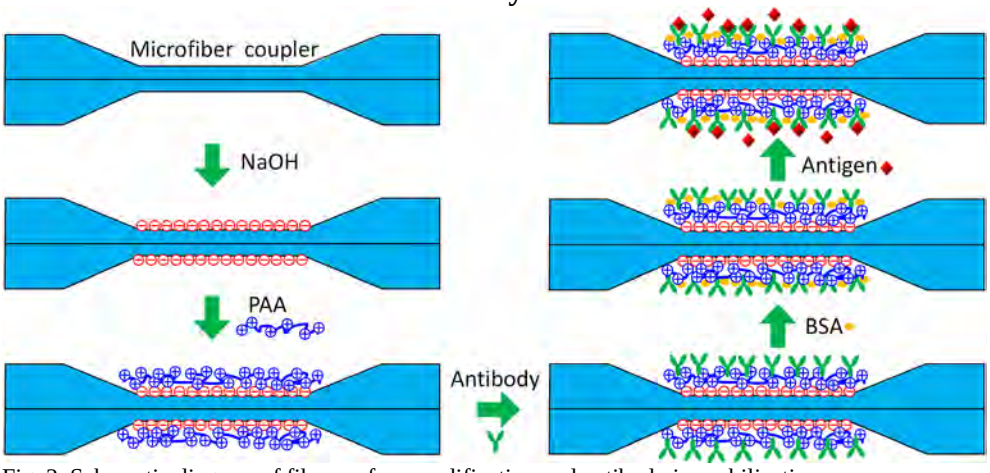

Fig. 2. Schematic diagram of fiber surface modification and antibody immobilization.

The process of fiber surface modification and antibody immobilization is shown in Fig. 2. In this study, we adopt the electrostatic adsorption strategy which has proven to be simple and effective to immobilize antibodies on the sensor surface [31,32]. The isoelectric point of the mouse monoclonal antibody is 7.0. Thus, it is negatively charged at pH 7.4 in PBS and can be adsorbed to the positively charged fiber surface. First, we treat the OMC surface with

NaOH solution (5 mM) for 10 mins to render the surface of the sensor negatively charged [33], followed by a thorough rinse with DI water to remove redundant NaOH residues. Second, we add PAA (0.5%) solution into the fluid cell to form a self-assembly monolayer of PAA on the fiber surface through electrostatic interaction, since PAA is positively charged. Afterward, we rinse the OMC thoroughly to remove the unbonded PAA molecules. Third, a layer of active cTnT antibodies is introduced to the fiber surface through electrostatic binding with PAA by injecting cTnT antibody solution (10 μg/mL) into the fluid channel. The binding process reaches saturation after about 2 hours and then we wash the fiber surface thoroughly with PBS solution to remove the unbonded antibodies. Fourth, to prevent non-specific binding, a BSA solution with the concentration of 1 mg/mL is added and incubated for 30 mins to block un-reacted binding sites, followed by a thorough rinse with PBS solution. Finally, the OMC is ready for cTnT molecule detection. During the surface modification and biomarker detection process, we inject the samples into the sensor cell and suck out the liquids using a pipette. The volume for each injection is 180 μL.

3. Results and discussions

3.1 Operation principle

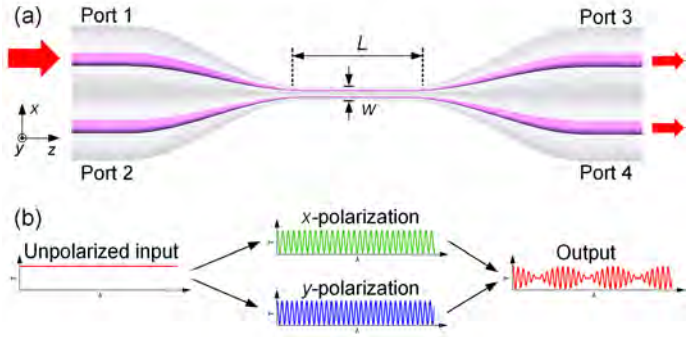

Fig. 3. (a) Schematic diagram of the OMC sensor. (b) Basic operation principle.

Fig. 3 shows the schematic structure of a typical OMC. It consists of a uniform waist region where two micro-fibers are closely packed, two input ports and two output ports. The two input ports are equivalent and here we chose port 1 as the input port. According to the supermode theory, the two parallel and neighboring microfibers in the waist region can be regarded as a new waveguide. When light in *x*-/*y*-polarization is launched from port 1, both even and odd supermodes are excited equally and simultaneously in the waist region. Coupling between these two modes occurs when they propagate along the waist. The working principle of our sensing scheme is illustrated in Fig. 3(b). As the OMC is highly birefringent, the mode interferences in *x*-polarization and *y*-polarization vary slightly as they propagate along the waist. Thus, the Vernier effect can be observed at the two output ports. The output powers are then obtained as [34]:

$$P_3 = P_{1x}\cos^2\left(\frac{1}{2}\phi_x\right) + P_{1y}\cos^2\left(\frac{1}{2}\phi_y\right) \quad (1)$$

$$P_4 = P_{1x}\sin^2\left(\frac{1}{2}\phi_x\right) + P_{1y}\sin^2\left(\frac{1}{2}\phi_y\right) \quad (2)$$

where P_{1x} and P_{1y} denote the input optical power at port 1 in *x*- and *y*-polarization, respectively, P_3 and P_4 represent the total output power at port 3 and port 4, respectively, ϕ_x and ϕ_y represent the phase differences between the even and odd supermodes accumulated along the coupling length for *x*- and *y*-polarizations, respectively. In fact, the phase difference

induced by the transition regions is much smaller than that by the waist region because of the larger geometric size. Thereby we can approximately express the phase term ϕ as [34]:

$$\phi_x = \frac{2\pi L(n^x_{\text{even}} - n^x_{\text{odd}})}{\lambda} \tag{3}$$

$$\phi_y = \frac{2\pi L(n^y_{\text{even}} - n^y_{\text{odd}})}{\lambda} \tag{4}$$

where n^x_{even}, n^x_{odd}, n^y_{even} and n^y_{odd} are the effective RIs of the even and odd supermodes in *x*-polarization and *y*-polarization, respectively. L and λ represent the length of the coupling region and wavelength. Assuming the incident light has equal optical power in both polarizations, e.g. $P_{1x} = P_{1y} = P_1/2$, by combining Eq. (1), (3) and (4), the output power at port 3 is:

$$P_3 = \frac{P_1}{2}\left(1 + \cos\left(\frac{\phi_x - \phi_y}{2}\right)\cos\left(\frac{\phi_x + \phi_y}{2}\right)\right) \tag{5}$$

Term $\cos\left(\frac{\phi_x - \phi_y}{2}\right)\cos\left(\frac{\phi_x + \phi_y}{2}\right)$ can be considered as a continuous wave carrier signal. Here we have $\phi_x + \phi_y > \phi_x - \phi_y$. Then, this carrier signal can be demodulated and we can obtain a carrier wave and message signal. The frequency of the carrier wave is much larger than the message signal. Thus the carrier wave and the message signal can be obtained as $\cos\left(\frac{\phi_x + \phi_y}{2}\right)$ and $\cos\left(\frac{\phi_x - \phi_y}{2}\right)$, or $-\cos\left(\frac{\phi_x + \phi_y}{2}\right)$ and $-\cos\left(\frac{\phi_x - \phi_y}{2}\right)$, respectively. Then, we can deduce the formula for the envelope function F_E through coordinate translation:

$$F_E = \frac{P_1}{2}\left(1 \pm \cos\left(\frac{\phi_x - \phi_y}{2}\right)\right) \tag{6}$$

Thus, the lower envelope function consisting of the dips can be expressed as:

$$F_c = \frac{P_1}{2}\left(1 - \left|\cos\left(\frac{\phi_x - \phi_y}{2}\right)\right|\right) = \frac{P_1}{2}\left(1 - \left|\cos\left(\frac{\pi L(\Delta n^x_{\text{eff}} - \Delta n^y_{\text{eff}})}{\lambda}\right)\right|\right) \tag{7}$$

where $\Delta n^x_{\text{eff}} = n^x_{\text{even}} - n^x_{\text{odd}}$, $\Delta n^y_{\text{eff}} = n^y_{\text{even}} - n^y_{\text{odd}}$. Similarly, the lower envelope function of the spectra from port 4 can also be deduced as Eq. (7), which indicates port 3 and port 4 can provide the same result when we employ the Vernier effect to improve the sensitivity. The N_{th} dip (here N is a positive integer) of the envelope satisfies:

$$\cos\left(\frac{\pi L(\Delta n^x_{\text{eff}} - \Delta n^y_{\text{eff}})}{\lambda_N}\right) = \cos\left(\frac{\pi L(B_{even} - B_{odd})}{\lambda_N}\right) = \pm 1 \tag{8}$$

where $B_{even} = n^x_{even} - n^y_{even}$, and $B_{odd} = n^x_{odd} - n^y_{odd}$ denote the birefringence of the even mode and the odd mode, respectively. Then we have:

$$\frac{\pi L(B_{even} - B_{odd})}{\lambda_N} = N\pi \tag{9}$$

By taking a small variation with respect to surrounding RI (SRI) from Eq. (9), the RI sensitivity of the Nth dip S_v can be deduced as:

$$S_v = \frac{\partial \lambda_N}{\partial n} = \frac{\lambda_N}{G_B^{even} - G_B^{odd}} \frac{\partial (B_{even} - B_{odd})}{\partial n} \tag{10}$$

Where $G_B^i = B_i - \lambda_N \partial B_i / \partial \lambda$ represents the group birefringence of the even mode or the odd mode, with i denotes even or odd mode. From Eq. (10), the sensitivity is determined by three terms: wavelength λ_N, $\frac{\partial (B_{even} - B_{odd})}{\partial n}$, and the difference between the group birefringence of the even mode and the odd mode. The sensitivity can be greatly enhanced when $G_B^{even} - G_B^{odd}$ approaches 0, i.e. the group birefringence of the even mode equals to that of the off mode. This condition can be achieved by optimizing the parameters of the OMC.

The RI sensitivity of the M_{th} interference dip (M is a positive integer) for the x-/y-polarization can be obtained as [35,36]:

$$S_i = \frac{\lambda_N}{n_{\text{g}}^{\text{even},\,j} - n_{\text{g}}^{\text{odd},\,j}} \frac{\partial\left(n_{\text{eff}}^{\text{even},\,j} - n_{\text{eff}}^{\text{odd},\,j}\right)}{\partial n} \tag{11}$$

where $n_{\text{g}}^{\text{even},\,j}$ and $n_{\text{g}}^{\text{even},\,j}$ denote the group effective index of the even mode and the odd mode, with j denotes x-/y-polarization. And $g = n_{\text{g}}^{\text{even},\,j} - n_{\text{g}}^{\text{odd},\,j}$ represents the difference between the group effective index of the even mode and the odd mode. From Eq. (11), the sensitivity is determined by three terms: wavelength λ_M, g and $\frac{\partial\left(n_{\text{eff}}^{\text{even},\,j} - n_{\text{eff}}^{\text{odd},\,j}\right)}{\partial n}$. The sensitivity can be greatly enhanced when g approaches 0, i.e. the group effective index of the even mode equals to that of the odd mode. This condition can also be achieved by optimizing the parameters of the OMC. Thus, with Eq. (10) and (11), we can draw a comparison on the RI sensing performance between the sensors with and without the Vernier effect.

3.2 Numerical analysis

First of all, to verify the effectiveness of the Vernier effect, we investigate the sensing performances of OMCs through numerical simulations. The effective indices of the even mode and odd mode in both x-polarization and y-polarization are calculated using a commercial software COMSOL Multiphysics 4.4. The RI of silica and water are obtained from Sellmeier-type dispersion formulas [37,38].

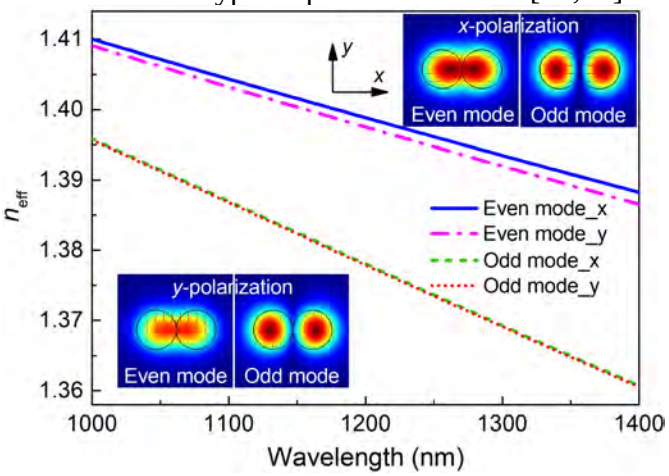

Fig. 4. Calculated effective RIs of the guided even and odd modes in x-polarization and y-polarization (insets show the modal fields of even and odd modes for both polarization; wavelength: 1200 nm).

Fig. 4 displays the effective RIs of the even and odd modes in both polarizations in the wavelength range of 1000 nm to 1400 nm for an OMC with a waist width of 3.2 μm. The insets show typical modal fields of the even and odd modes for both x-polarization and y-polarization. The results clearly show that the effective RI (n_{eff}) of even mode is slightly higher than that of odd mode for both x- and y-polarization states, and all the effective RIs become smaller towards longer wavelength. Furthermore, the effective RI of the even mode in x-polarization is obviously larger than that in y-polarization, whereas the effective RIs of odd modes in both polarizations are very close to each other. Thus, according to Eq. (6), we can infer that the even modes mainly contribute to the phase difference. Given the effective RIs, we can calculate the transmission spectrum with the Vernier effect at port 3 and the spectra of the lower envelope using Eq. (5) and (6), respectively. Fig. 55a shows the

calculated transmission spectra and lower envelopes of OMCs with different lengths of 10 mm, 20 mm, and 30 mm.

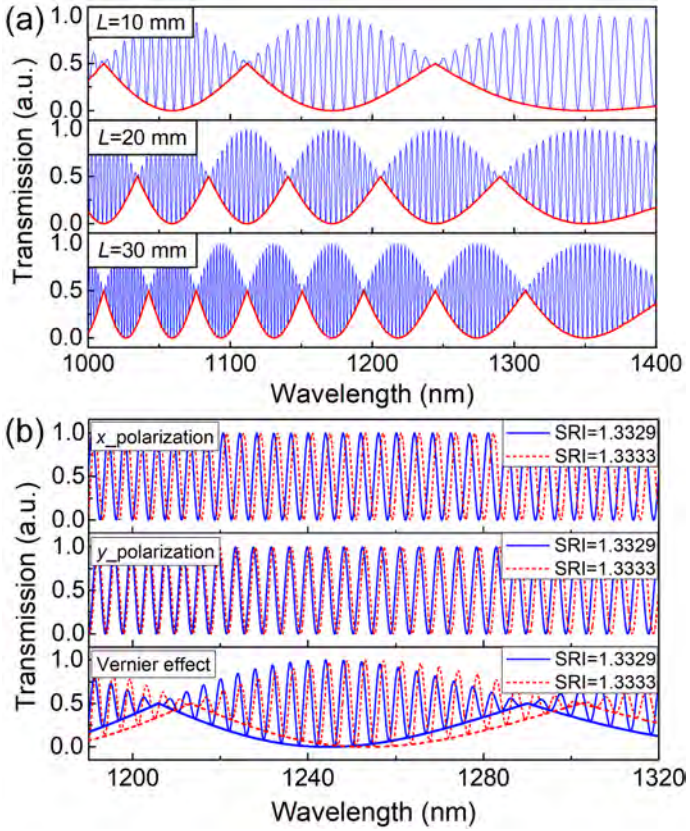

Fig. 5. (a) Calculated interference spectra with the Vernier effect for optical microfiber couples with different waist lengths (w=3.2 μm). (b) Calculated interference spectra for x-polarization, y-polarization and with the Vernier effect (w=3.2 μm).

To make a comparison, we analyze the spectral responses to SRI for both scenarios with and without the Vernier effect using an OMC with a width of 3.2 μm and a waist length of 12 mm as a model. As shown in Fig. 5b, when the SRI increases from 1.3329 to 1.3333, the transmission spectra for x-/y-polarizations without the Vernier effect show small changes that the interference dips only shift a little towards longer wavelengths. However, with the Vernier effect, the dips in the lower envelope exhibit a much stronger redshift with the same SRI increment, which demonstrates the significant contribution of the Vernier effect for sensitivity enhancement in OMC based RI sensors. Here, we take the parameter figure of merit (FOM) which defined as the ratio of the sensitivity S to the full width at half-maximum FWHM (FOM = S / FWHM) to evaluate the quality of the sensor [39]. Although the sensitivity can be enhanced, the broadening of the dips will enlarge the FWHM and cause FOM to decrease. However, according to Eq. 10 and 11, the sensitivity is independent on the length of the OMC for both scenarios with and without the Vernier effect. And according to Eq. 8, by increasing the coupler length L, the period in the lower envelope will decrease, which will, in turn, decrease the FWHM of the dip and further improve the FOM. Another difference between the OMC with and without the Vernier effect is that the data acquisition process is a bit more complicated for OMC sensors with the Vernier effect.

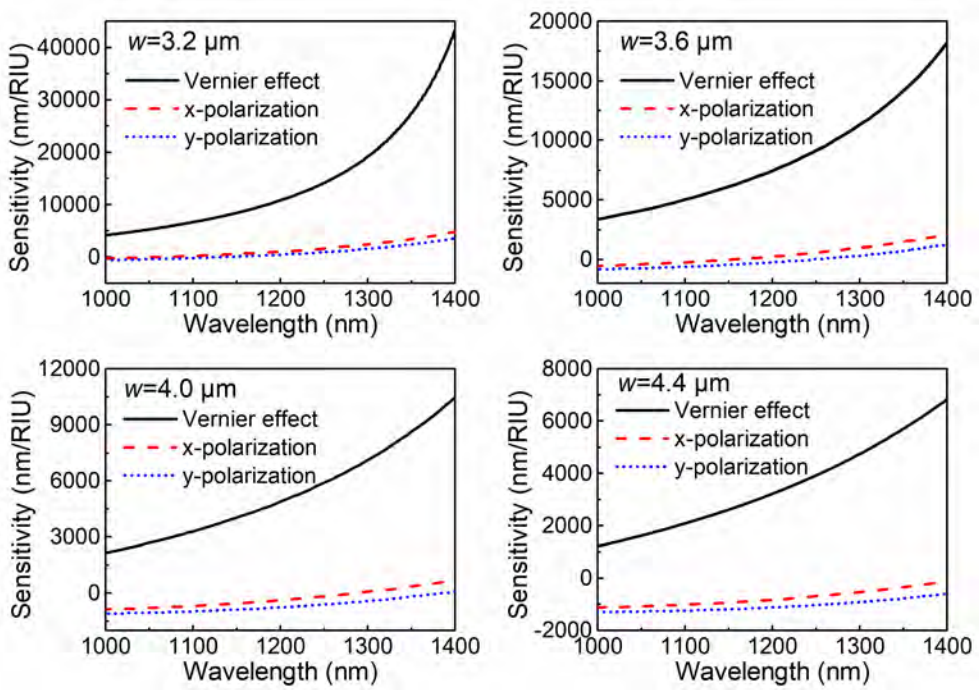

Fig. 6. Comparison of calculated sensitivities between OMCs with and without the Vernier effect. (w= 3.2~4.4 μm).

To analyze the sensitivity more comprehensively, we calculate the sensitivities for a group of OMCs with different waist widths. The results in Fig. 6 clearly show that the sensitivities are significantly enhanced for all the four couplers with the Vernier effect compared with the ones without the Vernier effect which only show very limited sensitivities on the order of few-thousand nm/RIU. In detail, with the Vernier effect, the sensitivity can reach nearly 40000 nm/RIU at long wavelengths for the 3.2 μm-wide coupler, and even for the 4.4 μm-wide coupler, the sensitivity can reach almost 8000 nm/RIU, which are much larger than those without the Vernier effect.

3.3 RI sensing demonstration

To experimentally verify the Vernier effect based sensing principle and to investigate the RI sensing performance, we use an OMC with a waist width of 3.2 μm and a waist length of ~12 mm. Optical micrographs of the fabricated OMC are shown in Fig. 7(a), and the transmission spectra of the OMC in air and DI water are shown in Fig. 7(b). The periodical envelope indicates the successful incorporation of the Vernier effect. The period of the envelope in DI water increases at longer wavelengths, which agrees well with the simulated spectra in Fig. 6(a). We also observe a broad dip at around 1450 nm which is attributed to the vibrational absorption of water molecules [40].

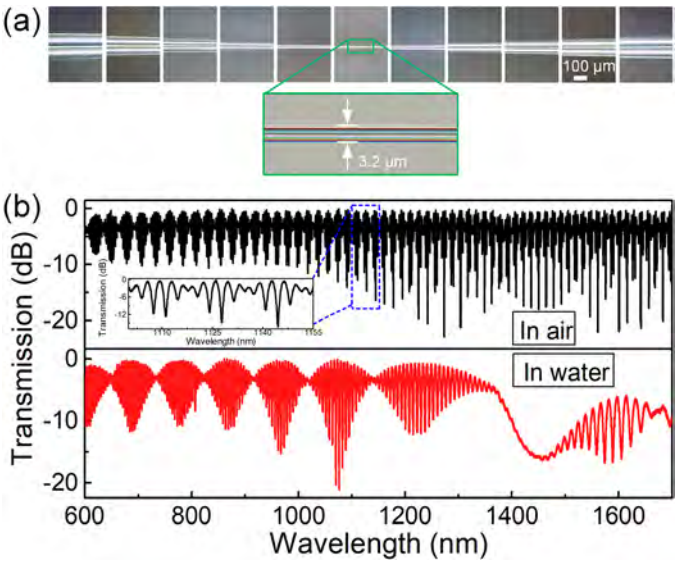

Fig. 7. (a) Micrographs of the fabricated OMC. (b) Transmission spectra of the OMC in air and in water.

First, we study the variation of interference spectra as SRI increases from 1.3330 to 1.3347 in small increments. The transmission spectra at port 3 together with the fitted curves for the lower envelopes are plotted in Fig. 8(a). As SRI gradually increases, all the dips in the envelope redshift and the dips at longer wavelengths tend to shift more. Then we measure the spectral responses of the OMC sensor when SRI increases from 1.3330 to 1.3488 with large increments. The transmission spectra together with the fitted curves for the lower envelopes are plotted in Fig. 8(b). When the SRI increases, distinct redshifts are observed for all the peaks along with the broadening of the dips. To analyze the RI sensitivity, we trace the wavelength shifts of dips A to D in the envelope as indicated in Fig. 8(a) and summarize the results in Fig. 8(c). The RI sensitivities of dips A, B, C and D at low RI range of 1.3330-1.3347 are calculated to be 7388.5 nm/RIU, 8189.9 nm/RIU, 12127.9 nm/RIU and 35823.3 nm/RIU, respectively, which are much larger than conventional fiber optic RI sensors. It is obvious that the dips at longer wavelength tend to show higher sensitivities. The RI sensitivity tends to increase nonlinearly as SRI further increases. The results also show that the dips at longer wavelengths exhibit higher sensitivities which agrees with the simulation results in Fig. 6. As a comparison, we investigate the RI sensing performance of the OMC operated in *x*-polarization state without the Vernier effect, and the RI sensitivities of the interference dips at similar positions with dips A, B, C and D are plotted in Fig. 8 (d). It is obvious that the sensitivities drop by almost one order of magnitude without the Vernier effect. Generally, optical fiber RI sensors with ultra-high sensitivities always show very limited dynamic ranges. So, in the application of such a sensor, we have evaluated the RI range to be measured first and then chose the appropriate dip. For RI with large variations, the dips at a short wavelength may be more suitable. However, for biosensing, where the change of the SRI is commonly very small, dips at longer wavelengths are preferable. As a result, this significantly enhanced RI sensing capability in the RI range of 1.33-1.35 where bioassays are typically carried out [41] is promising for highly sensitive biomolecule detections.

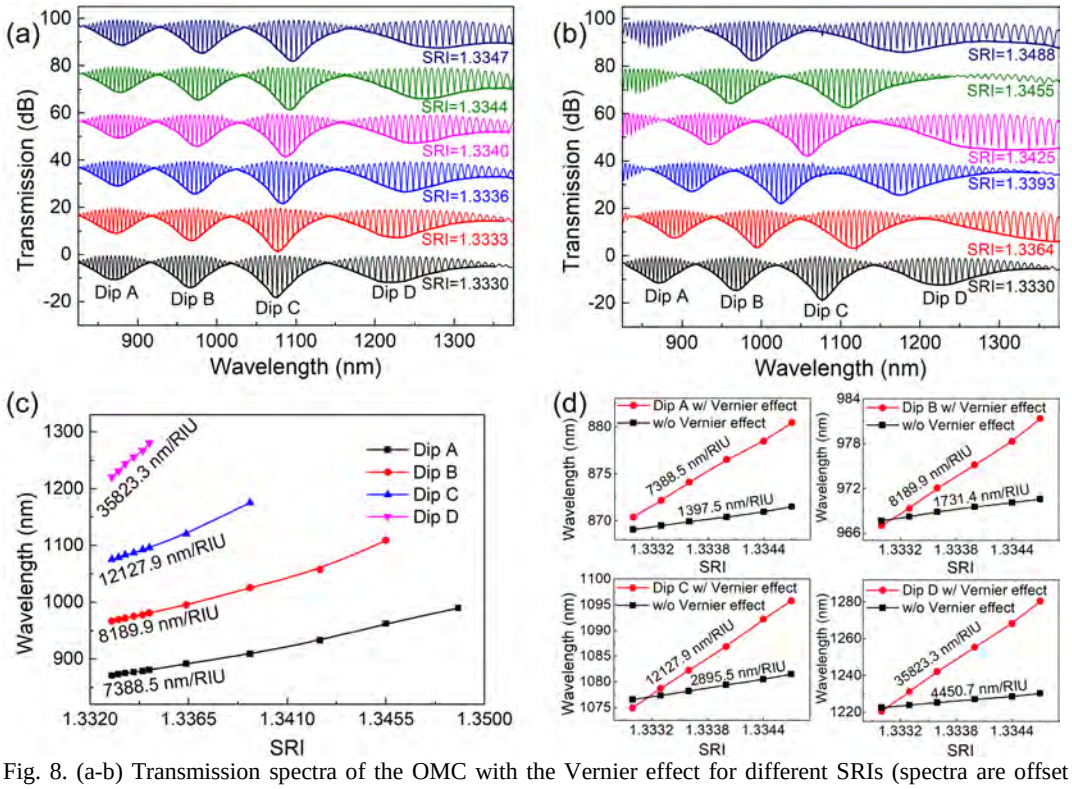

Fig. 8. (a-b) Transmission spectra of the OMC with the Vernier effect for different SRIs (spectra are offset by 22 dB for clarity). (c) Wavelength shift versus SRI for peaks A, B, C and D. (d) Comparison of the sensing performances of the same OMC with and without the Vernier effect.

3.4 Label-free biosensing of cTnT

The property of ultra-high RI sensitivity in the biological relevant RI range makes this Vernier effect assisted OMC a promising platform for chemical and biological sensing applications. As a proof of concept, we employ this sensor for cTnT protein detection to evaluate the effectiveness of the Vernier effect for sensing enhancement. cTnT is a cardio-specific, highly sensitive marker for myocardial damage and is immediately released to bloodstream during the acute myocardial infarction (AMI) [29]. The specific detection of cTnT protein is realized by introducing a single layer of specific antibodies onto the surface of the OMC to act as the bio-recognition element. The cTnT antibodies are immobilized on the fiber surface through electrostatic interactions following the procedure described in the materials and methods section. The transmission spectra after each step are recorded and the lower envelope for each spectrum is obtained. Fig. 9(a) shows the variation of the chosen dip during the surface modification. Distinct wavelength shifts are observed after each step, indicating the formation of each functional layer on the coupler surface. After the immobilization of cTnT antibodies and the blocking of the unbonded sites using BSA molecules, the sensor is ready for cTnT protein detection.

Different concentrations of cTnT protein solutions in PBS from 0.001 ng/ml to 1000 ng/mL are measured using the as-fabricated OMC biosensor to assess its biosensing performance. Prior to conducting specific bioassay, we first record the transmission spectrum of the as-fabricated OMC when it is immersed in PBS as the reference. The analyte solutions are injected in ascending order of concentration into the fluid channel and each is incubated for a duration of 20 mins to ensure saturation binding of cTnT molecules onto the antibodies

on the OMC surface, followed with a thorough rinsing with PBS to remove the unbonded molecules. After the rinsing procedure, the transmission spectrum for each concentration is measured and recorded. The fitted lower envelopes of the response spectra are shown in Fig. 9(b) and the inset shows an enlarged plot for the four lowest concentrations. It is clear that at low concentration of 0.001-0.1 ng/mL, the shifts of the dip are so small that they can be hardly distinguished. At higher concentration of 1-100 ng/mL the dip shifts to longer wavelengths with the increment of cTnT protein concentration, indicating more cTnT molecules are adsorbed to the fiber surface and lead to a steady increase of SRI around the OMC. Here we use the Hill function as an empirical model to fit the response data [42]. The Hill coefficient provides a way to quantify the degree of interaction between ligands and binding site and it is formally equivalent to the Langmuir isotherm. As shown in Fig. 9c, the fitted curve (R^2=0.99565) follows a sigmoidal behavior with a linear range of 0.1-100 ng/mL and reaches saturation after 100 ng/mL. We can obtain a limit of detection (LoD) of ~1 ng/mL by taking 3 times of the standard deviation.

In order to verify that the performance is enhanced by the Vernier effect in biomolecule detection, we conducted control experiments using an OMC with an identical width (L=3 mm). We plot the wavelength shifts for different concentrations of cTnT samples and the Hill function fitting (R^2=0.97465) in Fig. 9c for comparison. It is clear that the slope of the fitting curve for the sensor with the Vernier effect is much larger than that without the Vernier effect in the concentration range of 0.1-1000 ng/mL, indicating that the wavelength shifts are enlarged with the Vernier effect, and hence the sensing performance improved. To demonstrate the capability of the proposed sensor in real-time monitoring of the antibody-antigen binding process, we studied the real-time behavior of the sensor to a relatively high concentration of the analyte (1000 ng/mL). As depicted in Fig. 9d, the change of the wavelength shift show an increase in the binding event of cTnT molecules on to the sensor surface from 5-15 min and gradually saturated with time. Then we sucked out the sample and injected PBS to wash the unbounded cTnT molecules, which cause a little decrease in the wavelength shift.

Please note that the detection of cTnT only serves as a proof-of-concept to demonstrate the capability of the proposed sensor in biosensing and evaluate the effectiveness of the Vernier effect in biosensing enhancement in our study. We realize that the LoD is a bit higher than the relevant concentrations of cTnT in AMI patients. In order to improve the sensing performance, we can support the OMCs with a low-RI substrate to enhance the robustness and reduce the standard deviation of the measured signals. The immobilization strategy can be further optimized to improve the activity of the immobilized the antibodies, for example, using the covalent immobilization strategy or using the protein A/G to retain the activities of the antibodies at utmost [43]. Furthermore, optimization of the incubation temperature would also give rise to the sensing performance [44].

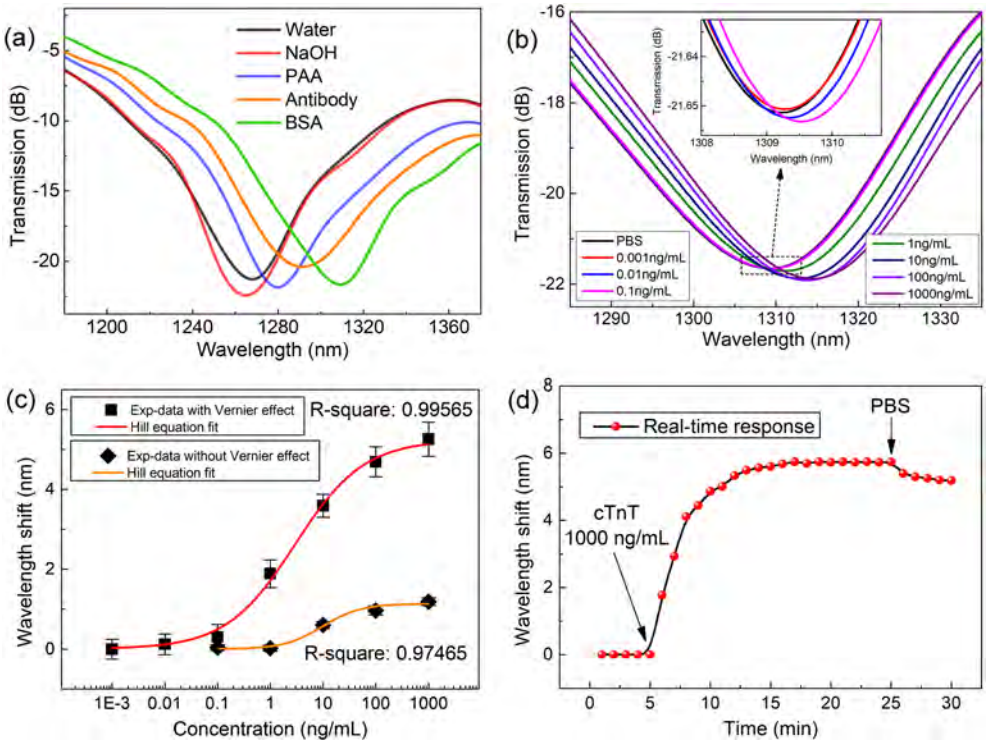

Fig. 9. (a) Fitted lower envelope from the transmission spectra at each step of surface modification and antibody immobilization. (b) Fitted lower envelope from the transmission spectra for deferent concentrations of cTnT protein. Inset: enlarged plots of the four lowest concentrations. (c) Comparison of the performance in bio-detection between OMCs with and without the Vernier effect. (d) The real-time response curve of the sensor to cTnT molecules (1000 ng/mL).

4. Conclusions

In this work, the birefringence induced Vernier effect in fiber-optic modal interferometers is proposed for sensitivity enhancement. Taking OMC as a model, we lay a theoretical foundation for the birefringence induced Vernier effect, and numerically study the spectral characteristics and RI sensing enhancement. Results show that with the Vernier effect, the RI sensitivities can be enhanced by nearly one order of magnitude by tracing the dips in the lower envelopes of the transmission spectra. Then we experimentally demonstrate that the RI sensitivity can be significantly enhanced in the RI range of 1.33-1.35 where bioassays are typically carried out using an OMC with a waist width of 3.2 μm, and an ultra-high RI sensitivity of 35823.3 nm/RIU around 1.333 is achieved. As a proof-of-concept, we use this sensor for human cTnT molecule detection to demonstrate the capability of the proposed sensor in biosensing and evaluate the effectiveness of the Vernier effect in biosensing enhancement in our study. With the help of the Vernier effect, the sensing performance is enhanced and a LoD of 1 ng/mL is achieved for human cTnT molecule. Although the LoD is a bit higher than the relevant concentrations of cTnT in AMI patients, we can envision the LoD to be much lower in the near future after optimizing the biology. The proposed biosensor has the advantage of speed over methods used in the clinical laboratories, which is promising for clinical applications. This sensor can also be implemented in other sensing applications such as temperature sensing, strain sensing, and magnetic field sensing, by pairing with the recent development of functional fibers [45-51]. More importantly, this sensing scheme offers a generic platform for optical fiber modal interferometers with birefringence.

Acknowledgments
This work was supported in part by the Singapore Ministry of Education Academic Research Fund Tier 2 (MOE2015-T2-1-066 and MOE2015-T2-2-010), Singapore Ministry of Education Academic Research Fund Tier 1 (RG85/16), and Nanyang Technological University (Start-up grant M4081515: Lei Wei).

Reference:

[1] K. Li, G. Liu, Y. Wu, P. Hao, W. Zhou, Z. Zhang, Gold nanoparticle amplified optical microfiber evanescent wave absorption biosensor for cancer biomarker detection in serum, Talanta. 120 (2014) 419–424. doi:10.1016/j.talanta.2013.11.085.

[2] N. Zhang, K. Li, Y. Cui, Z. Wu, P.P. Shum, J.-L. Auguste, X.Q. Dinh, G. Humbert, L. Wei, Ultra-sensitive chemical and biological analysis *via* specialty fibers with built-in microstructured optofluidic channels, Lab Chip. 18 (2018) 655–661. doi:10.1039/C7LC01247K.

[3] F. Long, M. He, A.N. Zhu, H.C. Shi, Portable optical immunosensor for highly sensitive detection of microcystin-LR in water samples, Biosens. Bioelectron. 24 (2009) 2346–2351. doi:10.1016/j.bios.2008.12.003.

[4] S.M. Tripathi, W.J. Bock, P. Mikulic, R. Chinnappan, A. Ng, M. Tolba, M. Zourob, Long period grating based biosensor for the detection of Escherichia coli bacteria, Biosens. Bioelectron. 35 (2012) 308–312. doi:10.1016/j.bios.2012.03.006.

[5] G. Liu, K. Li, Micro/nano optical fibers for label-free detection of abrin with high sensitivity, Sensors Actuators, B Chem. 215 (2015) 146–151. doi:10.1016/j.snb.2015.03.056.

[6] C. Liu, Q. Cai, B. Xu, W. Zhu, L. Zhang, J. Zhao, X. Chen, Graphene oxide functionalized long period grating for ultrasensitive label-free immunosensing, Biosens. Bioelectron. 94 (2017) 200–206. doi:10.1016/j.bios.2017.03.004.

[7] D. Sun, T. Guo, Y. Ran, Y. Huang, B.O. Guan, In-situ DNA hybridization detection with a reflective microfiber grating biosensor, Biosens. Bioelectron. 61 (2014) 541–546. doi:10.1016/j.bios.2014.05.065.

[8] M.A. Cooper, Label-free biosensors: Techniques and applications, 2009. doi:10.1017/CBO9780511626531.

[9] J. Pollet, F. Delport, K.P.F. Janssen, K. Jans, G. Maes, H. Pfeiffer, M. Wevers, J. Lammertyn, Fiber optic SPR biosensing of DNA hybridization and DNA-protein interactions, Biosens. Bioelectron. 25 (2009) 864–869. doi:10.1016/j.bios.2009.08.045.

[10] N.M.Y. Zhang, D.J.J. Hu, P.P. Shum, Z. Wu, K. Li, T. Huang, L. Wei, Design and analysis of surface plasmon resonance sensor based on high-birefringent microstructured optical fiber, J. Opt. 18 (2016) 065005. doi:10.1088/2040-8978/18/6/065005.

[11] N.M.Y. Zhang, K. Li, P.P. Shum, X. Yu, S. Zeng, Z. Wu, Q.J. Wang, K.T. Yong, L. Wei, Hybrid Graphene/Gold Plasmonic Fiber-Optic Biosensor, Adv. Mater. Technol. 2 (2017). doi:10.1002/admt.201600185.

[12] N.M.Y. Zhang, K. Li, T. Zhang, P. Shum, Z. Wang, Z. Wang, N. Zhang, J. Zhang, T. Wu, L. Wei, Electron-Rich Two-Dimensional Molybdenum Trioxides for Highly Integrated Plasmonic Biosensing, ACS Photonics. 5 (2018) 347–352. doi:10.1021/acsphotonics.7b01207.

[13] Y. Shao, S. Xu, X. Zheng, Y. Wang, W. Xu, Optical fiber LSPR biosensor prepared by gold nanoparticle assembly on polyelectrolyte multilayer, Sensors. 10 (2010) 3585–3596. doi:10.3390/s100403585.
[14] W. Bin Ji, H.H. Liu, S.C. Tjin, K.K. Chow, A. Lim, Ultrahigh sensitivity refractive index sensor based on optical microfiber, IEEE Photonics Technol. Lett. 24 (2012) 1872–1874. doi:10.1109/LPT.2012.2217738.
[15] K. Li, T. Zhang, G. Liu, N. Zhang, M. Zhang, L. Wei, Ultrasensitive optical microfiber coupler based sensors operating near the turning point of effective group index difference, Appl. Phys. Lett. 109 (2016) 101101. doi:10.1063/1.4961981.
[16] H. Tazawa, T. Kanie, M. Katayama, Fiber-optic coupler based refractive index sensor and its application to biosensing, Appl. Phys. Lett. 91 (2007) 113901. doi:10.1063/1.2783278.
[17] N. Zhang, G. Humbert, Z. Wu, K. Li, P.P. Shum, N.M.Y. Zhang, Y. Cui, J.-L. Auguste, X.Q. Dinh, L. Wei, In-line optofluidic refractive index sensing in a side-channel photonic crystal fiber, Opt. Express. 24 (2016) 419–424. doi:10.1364/OE.24.027674.
[18] N. Zhang, G. Humbert, T. Gong, P.P. Shum, K. Li, J.L. Auguste, Z. Wu, D.J.J. Hu, F. Luan, Q.X. Dinh, M. Olivo, L. Wei, Side-channel photonic crystal fiber for surface enhanced Raman scattering sensing, Sensors Actuators, B Chem. 223 (2016) 195–201. doi:10.1016/j.snb.2015.09.087.
[19] A. Leung, P.M. Shankar, R. Mutharasan, A review of fiber-optic biosensors, Sensors Actuators, B Chem. 125 (2007) 688–703. doi:10.1016/j.snb.2007.03.010.
[20] K.J. Lee, X. Liu, N. Vuillemin, R. Lwin, S.G. Leon-Saval, A. Argyros, B.T. Kuhlmey, Refractive index sensor based on a polymer fiber directional coupler for low index sensing, Opt. Express. 22 (2014) 17497. doi:10.1364/OE.22.017497.
[21] J. Wang, G. Liu, M.R. Jan, Ultrasensitive Electrical Biosensing of Proteins and DNA: Carbon-Nanotube Derived Amplification of the Recognition and Transduction Events, J. Am. Chem. Soc. (2004). doi:10.1021/ja031723w.
[22] M. Śmietana, M. Koba, P. Mikulic, W.J. Bock, Towards refractive index sensitivity of long-period gratings at level of tens of μm per refractive index unit: fiber cladding etching and nano-coating deposition, Opt. Express. 24 (2016) 11897. doi:10.1364/OE.24.011897.
[23] P. Pilla, C. Trono, F. Baldini, F. Chiavaioli, M. Giordano, A. Cusano, Giant sensitivity of long period gratings in transition mode near the dispersion turning point: an integrated design approach., Opt. Lett. 37 (2011) 4152–4154. doi:10.1016/j.bios.2011.05.048.
[24] J. Li, L. Sun, S. Gao, Z. Quan, Y. Chang, Y. Ran, L. Jin, B. Guan, Ultrasensitive refractive-index sensors based on rectangular silica microfibers, Opt. Lett. 36 (2011) 3593. doi:10.1364/OL.36.003593.
[25] H. Luo, Q. Sun, X. Li, Z. Yan, Y. Li, D. Liu, L. Zhang, Refractive index sensitivity characteristics near the dispersion turning point of the multimode microfiber-based Mach–Zehnder interferometer, Opt. Lett. 40 (2015) 5042. doi:10.1364/OL.40.005042.
[26] Z. Xu, Q. Sun, B. Li, Y. Luo, W. Lu, D. Liu, P.P. Shum, L. Zhang, Highly sensitive refractive index sensor based on cascaded microfiber knots with Vernier effect, Opt. Express. 23 (2015) 6662. doi:10.1364/OE.23.006662.

[27] E. Brzozowska, M. Koba, M. Śmietana, S. Górska, M. Janik, A. Gamian, W.J. Bock, Label-free Gram-negative bacteria detection using bacteriophage-adhesin-coated long-period gratings, Biomed. Opt. Express. 7 (2016) 829. doi:10.1364/BOE.7.000829.
[28] F. Chiavaioli, P. Biswas, C. Trono, S. Bandyopadhyay, A. Giannetti, S. Tombelli, N. Basumallick, K. Dasgupta, F. Baldini, Towards sensitive label-free immunosensing by means of turn-around point long period fiber gratings, Biosens. Bioelectron. 60 (2014) 305–310. doi:10.1016/j.bios.2014.04.042.
[29] A. Procopio, S. De Rosa, C. Covello, A. Merola, J. Sabatino, A. De Luca, C. Indolfi, F. Amato, C. Cosentino, A model of cardiac troponin T release in patient with acute myocardial infarction, 2017 56th IEEE Conf. Decis. Control. (2017) 1–6. doi:10.1109/CDC.2017.8263703.
[30] A. Felipe, G. Espíndola, H.J. Kalinowski, J.A.S. Lima, A.S. Paterno, Stepwise fabrication of arbitrary fiber optic tapers, Opt. Express. 20 (2012) 19893. doi:10.1364/OE.20.019893.
[31] S. Chen, L. Liu, J. Zhou, S. Jiang, Controlling antibody orientation on charged self-assembled monolayers, Langmuir. (2003). doi:10.1021/la026498v.
[32] Z. He, F. Tian, Y. Zhu, N. Lavlinskaia, H. Du, Long-period gratings in photonic crystal fiber as an optofluidic label-free biosensor, Biosens. Bioelectron. (2011). doi:10.1016/j.bios.2011.05.048.
[33] S. Korposh, S. James, R. Tatam, S. Lee, Fibre-Optic Chemical Sensor Approaches Based on Nanoassembled Thin Films : A Challenge to Future Sensor Technology, Curr. Dev. Opt. Fiber Technol. (2013) 585. doi:10.5772/53399.
[34] S.W. Yang, T.L. Wu, C.W. Wu, H.C. Chang, Numerical modeling of weakly fused fiber-optic polarization beamsplitters - Part II: The three-dimensional electromagnetic model, J. Light. Technol. 16 (1998) 691–696. doi:10.1109/50.664084.
[35] K. Li, N. Zhang, N.M.Y. Zhang, G. Liu, T. Zhang, L. Wei, Ultrasensitive measurement of gas refractive index using an optical nanofiber coupler, Opt. Lett. 43 (2018) 679–682. doi:10.1364/OL.43.000679.
[36] K. Li, N.M.Y. Zhang, N. Zheng, T. Zhang, G. Liu, L. Wei, Spectral Characteristics and Ultrahigh Sensitivities Near the Dispersion Turning Point of Optical Microfiber Couplers, J. Light. Technol. 36 (2018) 2409–2415. doi:10.1109/JLT.2018.2815558.
[37] I.H. Malitson, Interspecimen Comparison of the Refractive Index of Fused Silica*,†, J. Opt. Soc. Am. 55 (1965) 1205. doi:10.1364/JOSA.55.001205.
[38] S. Kedenburg, M. Vieweg, T. Gissibl, H. Giessen, Linear refractive index and absorption measurements of nonlinear optical liquids in the visible and near-infrared spectral region, Opt. Mater. Express. 2 (2012) 1588. doi:10.1364/OME.2.001588.
[39] C. Caucheteur, T. Guo, J. Albert, Review of plasmonic fiber optic biochemical sensors: improving the limit of detection, Anal. Bioanal. Chem. 407 (2015) 3883–3897. doi:10.1007/s00216-014-8411-6.
[40] K.F. Palmer, D. Williams, Optical properties of water in the near infrared*, J. Opt. Soc. Am. 64 (1974) 1107. doi:10.1364/JOSA.64.001107.
[41] D.A. Nagel, A. V Hine, L. Zhang, Label-free oligonucleotide biosensor based on dual-peak long period fiber grating, 9702 (2016) 1–6. doi:10.1117/12.2207869.

[42] B.I. Kurganov, A. V. Lobanov, I.A. Borisov, A.N. Reshetilov, Criterion for Hill equation validity for description of biosensor calibration curves, Anal. Chim. Acta. 427 (2001) 11–19. doi:10.1016/S0003-2670(00)01167-3.
[43] Y. Jung, J.Y. Jeong, B.H. Chung, Recent advances in immobilization methods of antibodies on solid supports, Analyst. (2008). doi:10.1039/b800014j.
[44] A.B. Mattos, T.A. Freitas, V.L. Silva, R.F. Dutra, A dual quartz crystal microbalance for human cardiac troponin T in real time detection, Sensors Actuators, B Chem. (2012). doi:10.1016/j.snb.2011.10.058.
[45] S. Shabahang, G. Tao, J. J. Kaufman, Y. Qiao, L. Wei, T. Bouchenot, A. Gordon, Y. Fink, Y. Bai, R.S. Hoy, A.F. Abouraddy, Controlled fragmentation of multimaterial fibres and films via polymer cold-drawing, Nature. 534 (2016) 529-533. doi:10.1038/nature17980.
[46] L. Wei, C. Hou, E. Levy, G. Lestoquoy, A. Gumennik, A.F. Abouraddy, J.D. Joannopoulos, Y. Fink, Optoelectronic fibers via selective amplification of in-fiber capillary instabilities, Advanced Materials. 29 (2017) 1603033. doi:10.1002/adma.201603033.
[47] L. Wei, T.T. Alkeskjold, A. Bjarklev, Tunable and rotatable polarization controller using photonic crystal fiber filled with liquid crystal, Applied Physics Letters. 96 (2010) 241104. doi:10.1063/1.3455105.
[48] T. Zhang, K. Li, J. Zhang, M. Chen, Z. Wang, S. Ma, N. Zhang, L. Wei, High-performance, flexible, and ultralong crystalline thermoelectric fibers, Nano Energy. 41 (2017) 35-42. doi:10.1016/j.nanoen.2017.09.019.
[49] C. Hou, X. Jia, L. Wei, A.M. Stolyarov, O. Shapira, J.D. Joannopoulos, Y. Fink, Direct atomic-level observation and chemical analysis of ZnSe synthesized by in situ high-throughput reactive fiber drawing, Nano Letters. 13 (2013) 975-979. doi: 10.1021/nl304023z.
[50] A.M. Stolyarov, L. Wei, F. Sorin, G. Lestoquoy, J.D. Joannopoulos, Y. Fink, Fabrication and characterization of fibers with built-in liquid crystal channels and electrodes for transverse incident-light modulation, Applied Physics Letters. 101 (2012) 011108. doi:10.1063/1.4733319.
[51] J. Zhang, K. Li, T. Zhang, P.J. Buenconsejo, M. Chen, Z. Wang, M. Zhang, Z. Wang, L. Wei, Laser induced in-fiber fluid dynamical instabilities for precise and scalable fabrication of spherical particles, Advanced Functional Materials. 27 (2017) 1703245. doi:10.1002/adfm.201703245.